



The Interior and Atmosphere of the Habitable-zone Exoplanet K2-18b

Nikku Madhusudhan , Matthew C. Nixon , Luis Welbanks , Anjali A. A. Piette , and Richard A. Booth

Institute of Astronomy, University of Cambridge, Madingley Road, Cambridge CB3 0HA, UK; nmadhu@ast.cam.ac.uk

Received 2019 September 27; revised 2020 January 28; accepted 2020 January 31; published 2020 February 27

Abstract

Exoplanets orbiting M-dwarfs present a valuable opportunity for their detection and atmospheric characterization. This is evident from recent inferences of H₂O in such atmospheres, including that of the habitable-zone exoplanet K2-18b. With a bulk density between Earth and Neptune, K2-18b may be expected to possess a H/He envelope. However, the extent of such an envelope and the thermodynamic conditions of the interior remain unexplored. In the present work, we investigate the atmospheric and interior properties of K2-18b based on its bulk properties and its atmospheric transmission spectrum. We constrain the atmosphere to be H₂-rich with a H₂O volume mixing ratio of 0.02%–14.8%, consistent with previous studies, and find a depletion of CH₄ and NH₃, indicating chemical disequilibrium. We do not conclusively detect clouds/hazes in the observable atmosphere. We use the bulk parameters and retrieved atmospheric properties to constrain the internal structure and thermodynamic conditions in the planet. The constraints on the interior allow multiple scenarios between rocky worlds with massive H/He envelopes and water worlds with thin envelopes. We constrain the mass fraction of the H/He envelope to be $\lesssim 6\%$; spanning $\lesssim 10^{-5}$ for a predominantly water world to $\sim 6\%$ for a pure iron interior. The thermodynamic conditions at the surface of the H₂O layer range from the supercritical to liquid phases, with a range of solutions allowing for habitable conditions on K2-18b. Our results demonstrate that the potential for habitable conditions is not necessarily restricted to Earth-like rocky exoplanets.

Unified Astronomy Thesaurus concepts: [Exoplanet atmospheres \(487\)](#); [Planetary interior \(1248\)](#); [Exoplanet atmospheric composition \(2021\)](#); [Exoplanet surface characteristics \(496\)](#); [Habitable planets \(695\)](#); [Habitable zone \(696\)](#)

1. Introduction

Recent exoplanet detection surveys have revealed high occurrence rates of low-mass planets orbiting M-dwarfs (Dressing & Charbonneau 2015; Mulders et al. 2015). The low masses, sizes, and temperatures of M-dwarfs also mean that the planet–star contrast is favorable for planetary detection and characterization. This “small-star opportunity” has led to several detections of low-mass planets ($< 10 M_{\oplus}$) in the habitable-zones of M-dwarf hosts such as Trappist-1 (Gillon et al. 2017), Proxima Centauri (Anglada-Escudé et al. 2016), K2-18 (Foreman-Mackey et al. 2015; Montet et al. 2015), and LHS 1140 (Dittmann et al. 2017).

The habitable-zone transiting exoplanet K2-18b is a particularly good example (Foreman-Mackey et al. 2015; Montet et al. 2015). The close proximity and small size of its host star make precise measurements of the planetary mass, radius, and atmospheric spectra viable (Benneke et al. 2017; Cloutier et al. 2019), as exemplified by the recent detection of H₂O in its atmosphere (Benneke et al. 2019; Tsiraras et al. 2019). The habitable-zone temperature of K2-18b provides further impetus for detailed characterization of its interior and atmosphere.

Given its mass ($M_p = 8.63 \pm 1.35 M_{\oplus}$; Cloutier et al. 2019) and radius ($R_p = 2.610 \pm 0.087 R_{\oplus}$; Benneke et al. 2019), K2-18b has a bulk density ($2.67_{-0.47}^{+0.52} \text{ g cm}^{-3}$; Benneke et al. 2019). This density, between that of Earth and Neptune, may be thought to preclude a purely rocky or icy interior and require a

hydrogen-rich outer envelope. However, the extent of such an envelope and the conditions at the interface between the envelope and the underlying interior have not been explored. We note that the mass and radius of the planet have recently been revised (Benneke et al. 2019), which may have impacted inferences made using previous values (Cloutier et al. 2017; Tsiraras et al. 2019).

Previous studies of planets with similar masses and radii, such as GJ 1214b, suggested envelope mass fractions $\lesssim 7\%$ (Rogers & Seager 2010; Nettelmann et al. 2011; Valencia et al. 2013). GJ 1214b is expected to host supercritical H₂O below the envelope at pressures and temperatures too high to be conducive for life (Rogers & Seager 2010). However, while GJ 1214b has an equilibrium temperature (T_{eq}) of ~ 500 K, K2-18b may be more favorable given its lower $T_{\text{eq}} \sim 250$ –300 K.

In the present work, we conduct a systematic study to constrain both the atmospheric and interior composition of K2-18b based on extant data along with detailed atmospheric retrievals and internal structure models.

2. Atmospheric Properties

We retrieve the atmospheric properties of K2-18b using its broadband transmission spectrum reported by Benneke et al. (2019). The data include observations from the *Hubble Space Telescope* (HST) WFC3 G141 grism (1.1–1.7 μm), photometry in the *Spitzer* IRAC 3.6 and 4.5 μm bands, and optical photometry in the K2 band (0.4–1.0 μm). We perform the atmospheric retrieval using an adaptation of the AURA retrieval code (Pinhas et al. 2019; Welbanks & Madhusudhan 2019). Our model solves line-by-line radiative transfer in a plane-parallel atmosphere in transmission geometry. The model assumes hydrostatic equilibrium and considers prominent

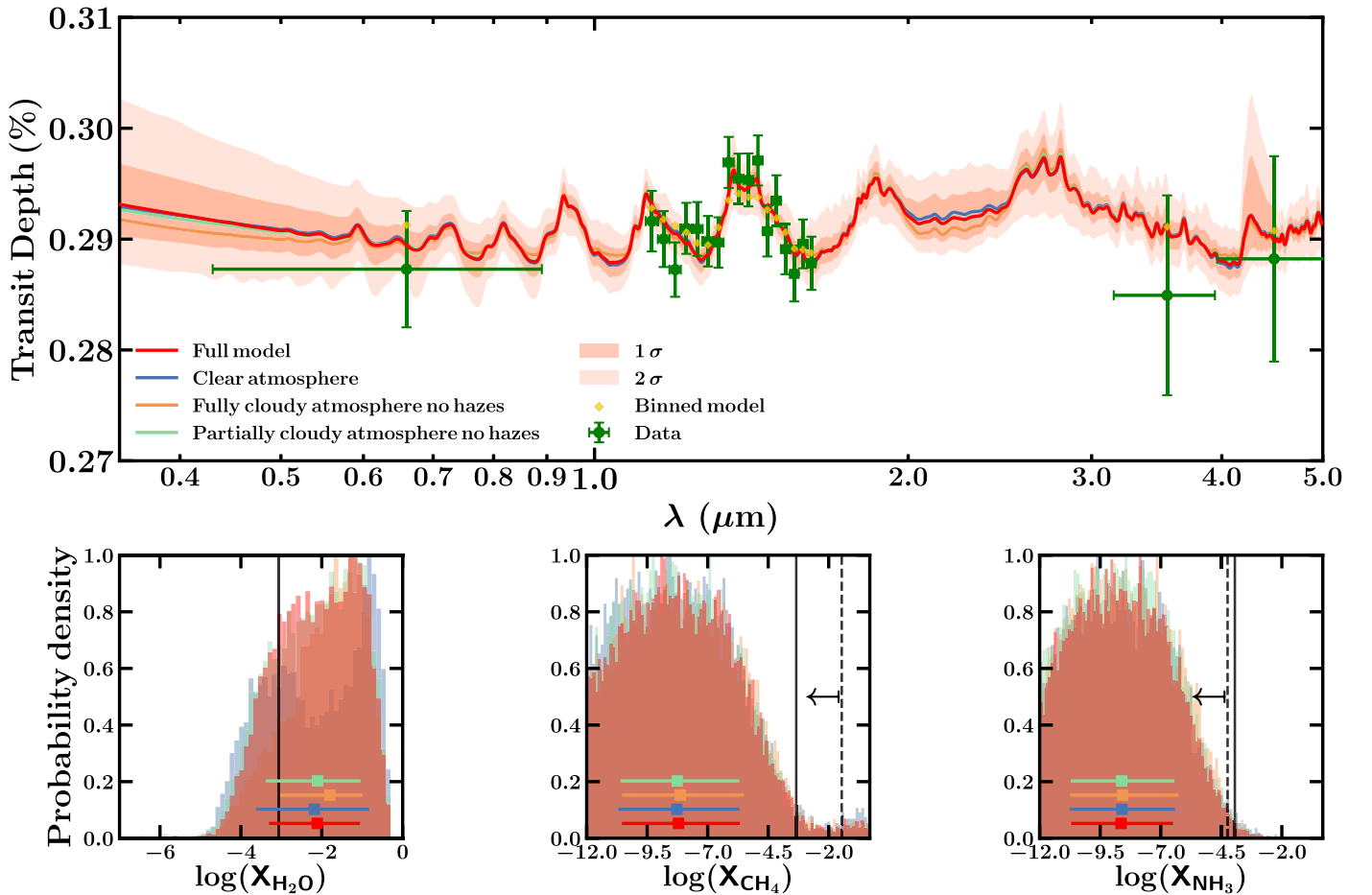


Figure 1. Atmospheric retrieval from the transmission spectrum of K2-18b. Top: observations (green) and retrieved model spectra for the four different model considerations in Table 1. Shaded regions represent 1σ and 2σ confidence intervals for the full model, with yellow points showing the model binned to the data resolution. The observations were adopted from Benneke et al. (2019). Bottom: posterior distributions for the retrieved volume mixing ratios of H_2O , CH_4 , and NH_3 . The 99% upper limits for the full model on CH_4 and NH_3 are shown by the arrows and dashed lines. Equilibrium solar values are shown by solid black lines.

opacity sources in the observed spectral bands as well as homogeneous/inhomogeneous cloud/haze coverage. Clouds are included through a gray cloud deck with cloud-top pressure (P_c) as a free parameter. Hazes are included as a modification to Rayleigh scattering through parameters for the scattering slope (γ) and a Rayleigh-enhancement factor (a). The opacity sources include H_2O (Rothman et al. 2010), CH_4 (Yurchenko & Tennyson 2014), NH_3 (Yurchenko et al. 2011), CO_2 (Rothman et al. 2010), HCN (Barber et al. 2014), and collision-induced absorption due to $\text{H}_2\text{-H}_2$ and $\text{H}_2\text{-He}$ (Richard et al. 2012).

The model comprises 16 free parameters: abundances of five molecules, six parameters for the pressure–temperature (P – T) profile, four cloud/haze parameters, and one parameter for the reference pressure P_{ref} at R_p (e.g., Welbanks et al. 2019). The Bayesian parameter estimation is conducted using the Nested Sampling algorithm MultiNest (Feroz et al. 2009) through PyMultiNest (Buchner et al. 2014). We conduct retrievals for four model configurations: (1) a full model including inhomogeneous clouds and hazes, (2) a clear atmosphere, (3) an atmosphere with an opaque cloud deck but no hazes, and (4) an atmosphere with inhomogeneous clouds but no hazes. The atmospheric constraints are shown in Figure 1 and Table 1.

We confirm the high-confidence detection of H_2O in an H_2 -rich atmosphere as reported by Benneke et al. (2019) and Tsiaras et al. (2019). Our abundance estimates are consistent to within 1σ between all four model configurations and with

Benneke et al. (2019). The derived H_2O volume mixing ratio ranges between 0.02% and 14.80%, with median values of 0.7–1.6% between the 4 model cases, as shown in Table 1. The case with an opaque cloud deck (a clear atmosphere) retrieves slightly higher (lower) H_2O abundances as expected (Welbanks & Madhusudhan 2019). Our derived H_2O abundance range corresponds to an O/H ratio of 0.2–176.8 \times solar, assuming all the oxygen is in H_2O as expected in H_2 -rich atmospheres at such low temperatures (Burrows & Sharp 1999). The median H_2O abundance is $9.3 \times$ solar for the full model, case 1. We cannot compare our results with Tsiaras et al. (2019) as their retrievals were based on only the *HST* WFC3 data and used older measurements of the planetary mass and radius, which could have biased their inferences.

We find a depletion of CH_4 and NH_3 in the atmosphere. For a H_2 -rich atmosphere at ~ 300 K, CH_4 and NH_3 are expected to be dominant carriers of carbon and nitrogen, respectively, in chemical equilibrium (Burrows & Sharp 1999), as also seen for the gas and ice giants in the solar system (Atreya et al. 2016). Assuming solar elemental ratios (i.e., $\text{C}/\text{O} = 0.55$, $\text{N}/\text{O} = 0.14$), the $\text{CH}_4/\text{H}_2\text{O}$ ($\text{NH}_3/\text{H}_2\text{O}$) ratio is expected to be ~ 0.5 (~ 0.1). However, we do not detect CH_4 or NH_3 despite their strong absorption in the *HST* WFC3 and/or *Spitzer* $3.6 \mu\text{m}$ bands. As shown in Figure 1, the retrieved posteriors of the CH_4 and NH_3 abundances are largely sub-solar, with 99% upper limits of 3.47×10^{-2} and 5.75×10^{-5} , respectively.

Table 1
Retrieved Atmospheric Properties from the Transmission Spectrum of K2-18b

Model	$\log(X_{\text{H}_2\text{O}})$	$\log(X_{\text{CH}_4})$	$\log(X_{\text{NH}_3})$	$\ln(\mathcal{Z})$	Detection Significance (DS)
Case 1: Full model, inhomogenous clouds and hazes	$-2.11^{+1.06}_{-1.19}$	$-8.20^{+2.53}_{-2.34}$	$-8.64^{+2.15}_{-2.06}$	179.15	Reference
No H ₂ O	N/A	$-1.11^{+0.53}_{-1.22}$	$-7.27^{+2.91}_{-2.92}$	175.30	3.25
Case 2: Clear atmosphere	$-2.18^{+1.35}_{-1.44}$	$-8.27^{+2.59}_{-2.42}$	$-8.60^{+2.19}_{-2.16}$	179.05	1.20
Case 3: Opaque cloud deck	$-1.80^{+0.81}_{-1.22}$	$-8.13^{+2.64}_{-2.41}$	$-8.57^{+2.30}_{-2.17}$	179.09	1.06
Case 4: Inhomogenous clouds	$-2.10^{+1.07}_{-1.28}$	$-8.26^{+2.56}_{-2.34}$	$-8.61^{+2.18}_{-2.10}$	179.41	N/A

Note. Four models are considered with different treatments of clouds and hazes. For each model, the volume mixing ratios ($\log(X_{\text{H}_2\text{O}})$, $\log(X_{\text{CH}_4})$, and $\log(X_{\text{NH}_3})$) are shown along with the Bayesian evidence ($\ln(\mathcal{Z})$) and DS. The DS is derived from the Bayesian evidence and a value below 2.0σ is considered weak (Trotta 2008). The preference of the reference model (case 1) over other models is quantified by the DS. For example, the DS for case 2 implies that case 1 is preferred over case 2 at 1.2σ . H₂O is detected at 3.25σ and clouds/hazes at only $\sim 1\sigma$.

These sub-solar values are in contrast to the largely super-solar H₂O, arguing against chemical equilibrium at solar elemental ratios.

We do not find strong evidence for clouds/hazes in the atmosphere. Our model preference for clouds/hazes, relative to the cloud-free case, is marginal (1.2σ) compared to Benneke et al. (2019; 2.6σ). Our retrieved cloud-top pressure (P_c) for the full case is weakly constrained to 0.1 mbar to 2 bar, close to the observable photosphere. Finally, we retrieve P_{ref} for the full case to be 12–174 mbar corresponding to R_p . The median value of 0.05 bar is used as the surface boundary condition, pressure P_0 , for the internal structure models in Section 3.1.

3. Internal Structure and Composition

In this section we use the observed bulk properties of K2-18b, namely the planetary mass (M_p), radius (R_p), and its atmospheric properties, to constrain its internal structure and thermodynamic conditions.

3.1. Internal Structure Model

We model the interior of the planet with a canonical four-layer structure. The model comprises a two-component Fe + rock core consisting of an inner Fe layer and an outer silicate layer, a layer of H₂O, and an outer H/He envelope. Such a model spans the possible internal structures and compositions of super-Earths and mini-Neptunes (e.g., Valencia et al. 2010, 2013; Rogers et al. 2011; Lopez & Fortney 2014), as well as terrestrial planets and ice giants in the solar system (Guillot & Gautier 2014). The mass fractions of the different components (x_{Fe} , x_{rock} , $x_{\text{H}_2\text{O}}$, x_{env}) are free parameters in the model and sum to unity. Our present model is adapted from a three-layer model for super-Earths from Madhusudhan et al. (2012) comprising of Fe, rock, and H₂O, with the H/He envelope added in the present work.

The model solves the standard internal structure equations of hydrostatic equilibrium and mass continuity assuming spherical symmetry. The equation of state (EOS) for each of the two inner layers is adopted from Seager et al. (2007), who use the Birch–Murnaghan EOS (Birch 1952) for Fe (Ahrens 2000) and MgSiO₃ perovskite (Karki et al. 2000). For the H₂O layer we use the temperature-dependent H₂O EOS compiled by Thomas & Madhusudhan (2016) from French et al. (2009), Sugimura et al. (2010), Fei et al. (1993), Seager et al. (2007), and Wagner & Pruß (2002). For the gaseous envelope we use the latest H/He EOS from Chabrier et al. (2019) for a solar helium mass fraction ($Y = 0.275$).

The EOS in the H/He and H₂O layers can have a significant temperature dependence, which we consider in our model. Past studies (Rogers et al. 2011; Valencia et al. 2013) considered analytic P – T profiles for irradiated atmospheres derived using double gray approximations (Hansen 2008; Guillot 2010) with the internal and external fluxes and opacities as free parameters. We calculate self-consistent dayside P – T profiles for K2-18b in the H/He envelope using the GENESIS code (Gandhi & Madhusudhan 2017). GENESIS solves line-by-line radiative transfer under assumptions of hydrostatic, radiative-convective, and thermochemical equilibrium. We include opacity due to H₂O (Rothman et al. 2010), as detected in the transmission spectrum (Section 2), H₂ Rayleigh scattering, clouds and H₂–H₂ and H₂–He collision-induced absorption. We use an H₂O abundance of $10 \times$ solar (see Section 2) and also use $10 \times$ solar abundances for the cloud species. We include KCl, ZnS, and Na₂S clouds (Morley et al. 2013), for which we obtain opacities from Pinhas & Madhusudhan (2017). We further include water ice clouds using opacities from Budaj et al. (2015).

The P – T profile also depends on the planetary internal flux, which is characterized by the internal temperature T_{int} . We consider values of T_{int} which span the range expected for a planet with the mass and radius of K2-18b and an age of 1–10 Gyr, with envelope compositions from solar to water-rich. We choose end-member cases of $T_{\text{int}} = 25$ and 50 K, consistent with previous studies on planets of similar mass and radius, e.g., GJ 1214b (e.g., Valencia et al. 2013). The GENESIS models are calculated between pressures of 10^{-5} – 10^3 bar, and assume full redistribution of the incident stellar irradiation. We explore a range of P – T profiles and choose two representative cases, with different T_{int} , discussed further in Sections 3.2 and 3.3. Where required by the internal structure model, the bottom of the P – T profile of the H/He envelope is continued to deeper pressures using the adiabatic gradient from Chabrier et al. (2019). We also employ an adiabatic temperature profile in the H₂O layer, following Thomas & Madhusudhan (2016).

3.2. Constraints on Interior Composition

Figure 2 shows mass–radius (M – R) relations for models with different interior compositions. We explore the full range of plausible interior compositions in three components: $x_{\text{core}} = x_{\text{Fe}} + x_{\text{rock}}$, $x_{\text{H}_2\text{O}}$, and x_{env} , where $x_i = M_i/M_p$ is the mass fraction of each component i . For each atmospheric P – T profile considered, we explore two different core compositions: (1) an Earth-like core made of 33% Fe, 67% rock by mass, and (2) a

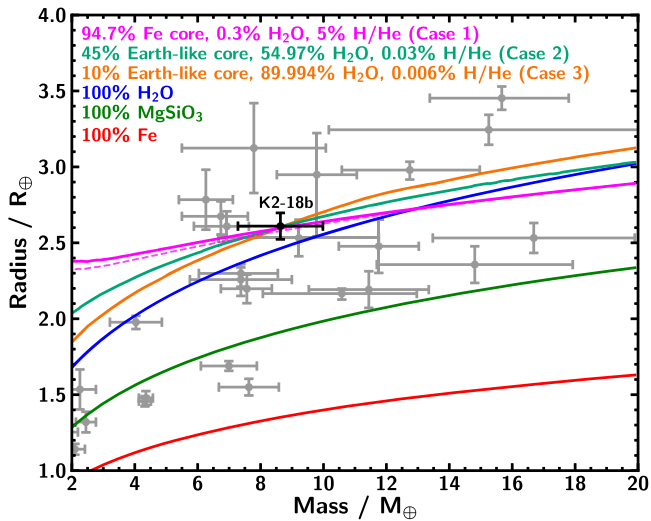


Figure 2. Model M - R relations for planets with different compositions. The mass fractions are shown in the legend. The solid magenta, teal, and orange curves show cases with three representative compositions, discussed in Section 4.1, that all fit the mass and radius of K2-18b equally well. The dashed magenta line represents the same composition as the solid magenta line, but with a mixed H_2O - H/He envelope. Also shown are exoplanets whose masses and radii are known to $\geq 3\sigma$ with $T_{\text{eq}} < 1000$ K, from TEPcat (Southworth 2011).

pure Fe core, the densest possible composition. Here, we discuss results from two end-member cases: (1) a pure Fe core with $T_{\text{int}} = 25$ K, and (2) an Earth-like (33% Fe) core with $T_{\text{int}} = 50$ K. Solutions for all other cases lie between these two cases.

As shown in Figure 3, while a wide range of core and H_2O mass fractions are permitted, we place a stringent upper limit on the mass fraction of the H/He envelope: $x_{\text{env}} = 6.2\%$. This maximal x_{env} corresponds to the case of a pure Fe core, with $x_{\text{core}} \sim 94\%$, underlying the H/He envelope with no $x_{\text{H}_2\text{O}}$; here it is assumed that the atmospheric H_2O is not mixed in the envelope. However, if the retrieved atmospheric H_2O abundance is assumed to be well mixed in the envelope then the maximal $x_{\text{env}} = 6\%$ with $x_{\text{H}_2\text{O}} = 0.4\%$ by mass; low, but still significantly higher than that of the Earth’s oceans ($\sim 0.02\%$).

We find that a substantial gaseous H/He envelope is not necessary to explain the density of K2-18b. Figure 3 shows the x_{env} required for different x_{core} . At one extreme, a $\sim 100\%$ H_2O interior with no rocky core can explain the data with an x_{env} of just $\sim 10^{-6}$, comparable to the mass fraction of the Earth’s atmosphere. The presence of a rocky core would necessitate at least a thin H/He envelope. However, even considering a reasonable $x_{\text{core}} = 10\%$ – 50% still requires x_{env} of only $\sim 10^{-5}$ – 10^{-2} , as shown in Figure 3. Model solutions with the hotter P - T profile and/or lower Fe content in the core require smaller x_{env} for a given x_{core} .

We have also considered models with miscible H_2O and H/He envelopes. We follow the approach of Soubiran & Militzer (2015), using an additive volume law for mixtures. Assuming that the median H_2O mixing ratio in the atmosphere is representative of the mixed (H_2O - H/He) envelope, we find that the difference in radius between the mixed and non-mixed models is less than half of the measured uncertainty (see Figure 2). The constraint on the envelope mass fraction from this mixed case is $x_{\text{env}} = 2.5\%$ – 6.4% , consistent with, and a subset of, the constraints discussed above. Note that in this case x_{env} includes both the H/He and H_2O mass fraction.

3.3. Atmosphere–Ocean Boundary

Our constraints on the interior compositions of K2-18b result in a wide range of thermodynamic conditions at the H_2O - H/He boundary (HHB). The pressure (P_{HHB}) and temperature (T_{HHB}) at the HHB for the model solutions are shown in Figure 4. Each point on the HHB loci denotes the transition from the P - T profile in the H/He envelope to the corresponding H_2O adiabat. The P_{HHB} and T_{HHB} depend on the H/He envelope mass fraction. For a given P - T profile, larger envelopes result in higher P_{HHB} and T_{HHB} . For example, solutions with $x_{\text{env}} \gtrsim 1\%$ lead to P_{HHB} and T_{HHB} corresponding to the supercritical phase of H_2O . As shown in Figure 3, solutions with higher x_{env} correspond to higher x_{core} and lower $x_{\text{H}_2\text{O}}$.

Conversely, solutions with lower x_{core} and, hence, lower x_{env} and higher $x_{\text{H}_2\text{O}}$, lead to lower P_{HHB} and T_{HHB} with H_2O in vapor or liquid phases at the HHB. For example, an $x_{\text{core}} \lesssim 30\%$ leads to a P_{HHB} and T_{HHB} corresponding to the liquid phase of H_2O , for the cooler P - T profile (with $T_{\text{int}} = 25$ K). For $x_{\text{core}} \sim 10\%$ or less, the P_{HHB} and T_{HHB} approach STP conditions for liquid H_2O . Below the HHB, H_2O is found in increasingly dense phases spanning liquid, vapor, supercritical, and ice states depending on the location of the HHB and the extent of the H_2O layer, as shown in Figure 4. In the case of a mixed H_2O - H/He envelope, the HHB is undefined as it corresponds to an extreme case with no pure H_2O layer.

4. Discussion

Our constraints on the interior and atmospheric properties of K2-18b provide insights into its physical conditions, origins, and potential habitability.

4.1. Possible Compositions and Origins

Here we discuss three representative classes that span the range of possible compositions, as indicated in Figures 2–4. The specific cases chosen here fit the M_p and R_p exactly, as shown in Figure 2. A wider range of solutions exist in each of these classes within the 1σ uncertainties.

Case 1: Rocky World. One possible scenario is a massive rocky interior overlaid by a H/He envelope. For example, a pure Fe core of 94.7% by mass with an almost maximal H/He envelope of 5% explains the data with minimal $x_{\text{H}_2\text{O}} = 0.3\%$, consistent with our retrieved H_2O abundance in the atmosphere. The HHB in this case is at $\sim 10^6$ bar, yielding supercritical H_2O close to the ice X phase. It is also possible in this case that the H_2O and H/He are mixed, meaning the HHB is not well defined. Such a scenario is consistent with either H_2 outgassing from the interior (Elkins-Tanton & Seager 2008; Rogers & Seager 2010) or accretion of an H_2 -rich envelope during formation (Lee & Chiang 2016).

Case 2: Mini-Neptune. There are a range of plausible compositions consisting of a non-negligible H/He envelope in addition to significant H_2O and core mass fractions, akin to canonical models for Neptune and Uranus (Guillot & Gautier 2014). One such example is a 45% Earth-like core with $x_{\text{env}} = 0.03\%$ and $x_{\text{H}_2\text{O}} = 54.97\%$. In this case the HHB is at $P_{\text{HHB}} = 700$ bar and $T_{\text{HHB}} = 1500$ K, with H_2O in the supercritical phase.

Case 3: Water World. A $\sim 100\%$ water world with a minimal H_2 -rich atmosphere ($x_{\text{env}} \sim 10^{-6}$) is permissible by the data.

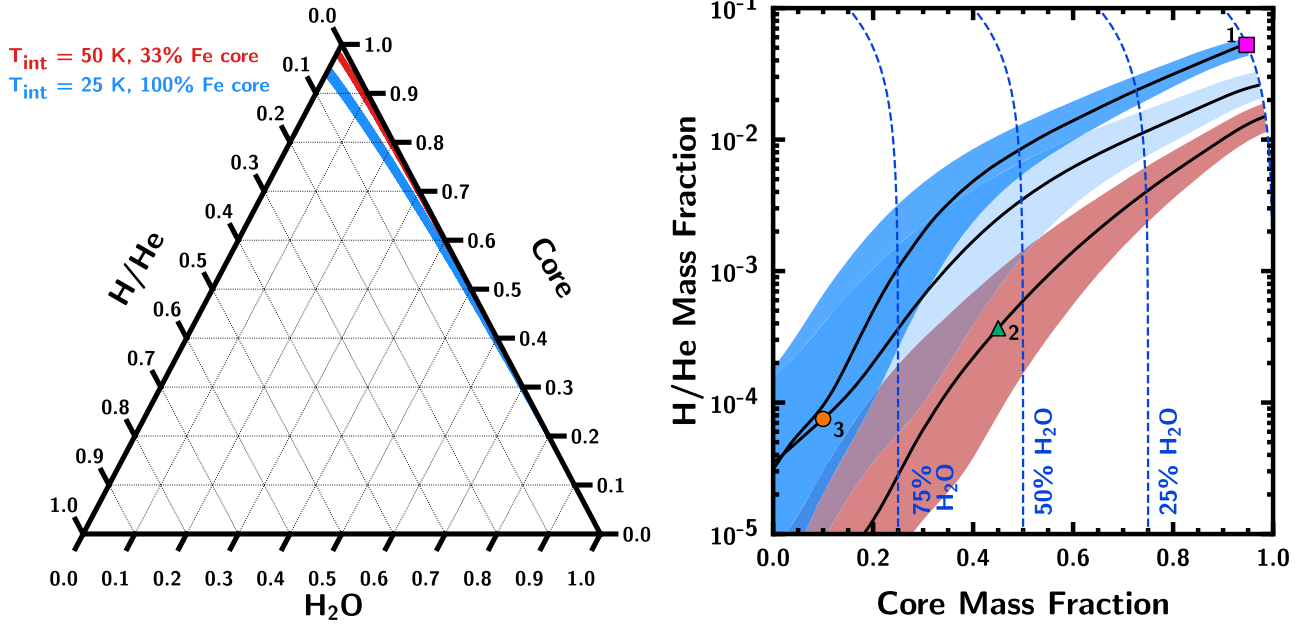


Figure 3. Left: ternary diagram showing best-fitting ($\leq 1\sigma$) interior compositions allowed by the mass and radius of K2-18b for two end-member core compositions and interior temperatures. Right: envelope vs. core mass fraction for model solutions. The dark red and blue shaded regions show the same cases as in the ternary diagram. The pale blue region shows an additional case with $T_{\text{int}} = 25 \text{ K}$ and an Earth-like core for comparison. The black lines in each case show the loci of the best-fit solutions. The magenta square, teal triangle, and orange circle represent the rocky world, intermediate and water world scenarios discussed in Section 4. The H/He mass fraction (x_{env}) is constrained to be $< 3.3\%$ ($< 6.2\%$) for models with an Earth-like (33% Fe) core and a pure (100%) Fe core, respectively.

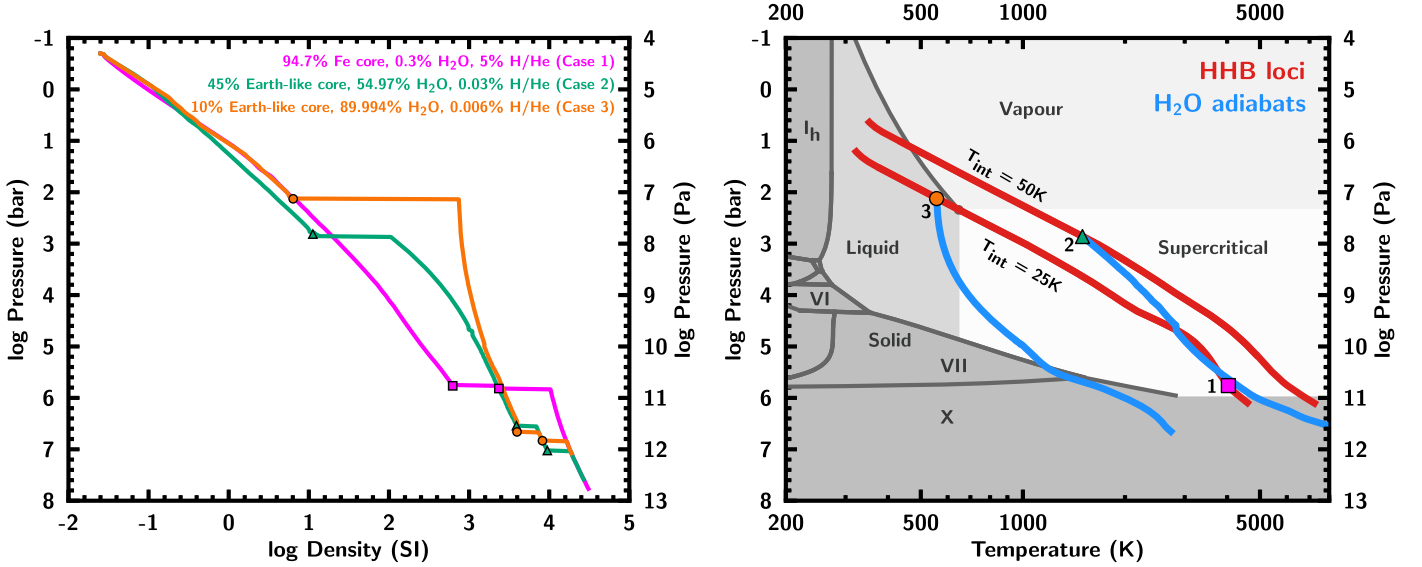


Figure 4. Left: pressure–density profiles for three possible compositions of K2-18b discussed in Section 4. The transitions between components are marked. Right: thermodynamic conditions at the HHB. The red lines indicate the range of possible pressures and temperatures at the HHB for two values of T_{int} considered. They trace the two model P – T profiles in the H/He layer. For each case the models span both Earth-like and Fe-only core compositions. The phase diagram of H₂O is shown in the background. The square, circle, and triangle correspond to the representative cases from the left-hand panel with the same color. We only show solutions with reasonable core mass fractions ($\geq 10\%$); less-massive cores lead to lower P and T at the HHB. The blue lines show the adiabatic temperature profiles in the H₂O layer below the HHB for the three examples.

However, such an extreme case is implausible from a planet formation perspective; some amount of rocky core is required to initiate further ice and gas accretion (Léger et al. 2004; Rogers et al. 2011; Lee & Chiang 2016). For example, a planet with $x_{\text{core}} = 10\%$, $x_{\text{H}_2\text{O}} = 89.994\%$ and a thin H/He envelope ($x_{\text{env}} = 0.006\%$) can explain the data. For this case, $P_{\text{HHB}} = 130 \text{ bar}$ and $T_{\text{HHB}} = 560 \text{ K}$, corresponding to liquid H₂O. For the same core fraction, solutions with even smaller H/He envelopes are admissible within the 1σ uncertainties on M_p and

R_p , leading to P_{HHB} and T_{HHB} approaching habitable STP conditions.

4.2. Potential Habitability

A notional definition of habitability argues for a planetary surface with temperatures and pressures conducive to liquid H₂O (e.g., Kasting et al. 1993; Meadows & Barnes 2018). Living organisms are known to thrive in Earth’s extreme

environments (extremophiles). Their living conditions span the phase space of liquid H₂O up to ~ 1000 bar pressures at the bottom of the Marianas Trench and ~ 400 K temperatures near hydrothermal vents (e.g., Merino et al. 2019).

Whether or not habitable conditions prevail on K2-18b depends on the extent of the H/He envelope. The thermodynamic conditions at the surface of the H₂O layer span a wide range in the H₂O phase diagram. While most of these solutions lie in the supercritical phase, many others lie in the liquid and vapor phases. Model solutions with core mass fractions $< 15\%$ and H/He envelopes $\lesssim 10^{-3}$ allow for liquid H₂O at Earth-like habitable conditions discussed above. One plausible scenario is an ocean world, as discussed in Section 4.1, with liquid water approaching STP conditions (e.g., 300 K, ~ 1 –10 bar) underneath a thin H/He atmosphere ($x_{\text{env}} \lesssim 10^{-5}$).

A number of studies in the past have argued for potential habitability on planets with H/He-rich atmospheres orbiting M-dwarfs (e.g., Pierrehumbert & Gaidos 2011; Seager et al. 2013; Koll & Cronin 2019). Given our constraints above, we find that K2-18b has a realistic chance of being habitable. Furthermore, our constraints on CH₄ and NH₃ suggest chemical disequilibrium. Among other possibilities for chemical disequilibrium, e.g., photochemistry, the potential influence of biochemical processes may not be entirely ruled out. Future observations, e.g., with the *James Webb Space Telescope*, will have the potential to refine our findings. We argue that planets such as K2-18b can indeed have the potential to approach habitable conditions and searches for biosignatures should not necessarily be restricted to smaller rocky planets.

N.M., M.N., A.P., and R.B. acknowledge support from the UK Science and Technology Facilities Council (STFC). L.W. thanks the Gates Cambridge Trust for support toward his doctoral studies. We thank the anonymous reviewer for helpful comments on the manuscript. This research is made open access thanks to the Bill & Melinda Gates foundation.


ORCID iDs

Nikku Madhusudhan  <https://orcid.org/0000-0002-4869-000X>

Matthew C. Nixon  <https://orcid.org/0000-0001-8236-5553>

Luis Welbanks  <https://orcid.org/0000-0003-0156-4564>

Anjali A. A. Piette  <https://orcid.org/0000-0002-4487-5533>

Richard A. Booth  <https://orcid.org/0000-0002-0364-937X>

References

Ahrens, T. J. 2000, *Mineral Physics & Crystallography: A Handbook of Physical Constants* (Washington, DC: American Geophysical Union)

Anglada-Escudé, G., Amado, P. J., Barnes, J., et al. 2016, *Natur*, **536**, 437

Atreya, S. K., Crida, A., Guillot, T., et al. 2016, in *Saturn in the 21st Century*, ed. K. H. Baines et al. (Cambridge: Cambridge Univ. Press), 5

Barber, R. J., Strange, J. K., Hill, C., et al. 2014, *MNRAS*, **437**, 1828

Benneke, B., Werner, M., Petigura, E., et al. 2017, *ApJ*, **834**, 187

Benneke, B., Wong, I., Piaulet, C., et al. 2019, *ApJL*, **887**, L14

Birch, F. 1952, *JGR*, **57**, 227

Buchner, J., Georgakakis, A., Nandra, K., et al. 2014, *A&A*, **564**, A125

Budaj, J., Kocifaj, M., Salmeron, R., & Hubeny, I. 2015, *MNRAS*, **454**, 2

Burrows, A., & Sharp, C. M. 1999, *ApJ*, **512**, 843

Chabrier, G., Mazevet, S., & Soubiran, F. 2019, *ApJ*, **872**, 51

Cloutier, R., Astudillo-Defru, N., Doyon, R., et al. 2017, *A&A*, **608**, A35

Cloutier, R., Astudillo-Defru, N., Doyon, R., et al. 2019, *A&A*, **621**, A49

Dittmann, J. A., Irwin, J. M., Charbonneau, D., et al. 2017, *Natur*, **544**, 333

Dressing, C. D., & Charbonneau, D. 2015, *ApJ*, **807**, 45

Elkins-Tanton, L. T., & Seager, S. 2008, *ApJ*, **685**, 1237

Fei, Y., Mao, H., & Hemley, R. J. 1993, *JChPh*, **99**, 5369

Feroz, F., Hobson, M. P., & Bridges, M. 2009, *MNRAS*, **398**, 1601

Foreman-Mackey, D., Montet, B. T., Hogg, D. W., et al. 2015, *ApJ*, **806**, 215

French, M., Mattsson, T. R., Nettelmann, N., & Redmer, R. 2009, *PhRvB*, **79**, 054107

Gandhi, S., & Madhusudhan, N. 2017, *MNRAS*, **472**, 2334

Gillon, M., Triaud, A. H. M. J., Demory, B.-O., et al. 2017, *Natur*, **542**, 456

Guillot, T. 2010, *A&A*, **520**, A27

Guillot, T., & Gautier, D. 2014, in *Treatise on Geophysics*, ed. T. Spohn & G. Schubert (2nd ed.; Amsterdam: Elsevier), 529

Hansen, B. M. S. 2008, *ApJS*, **179**, 484

Karki, B. B., Wentzcovitch, R. M., de Gironcoli, S., & Baroni, S. 2000, *PhRvB*, **62**, 14750

Kasting, J. F., Whitmire, D. P., & Reynolds, R. T. 1993, *Icar*, **101**, 108

Koll, D. D. B., & Cronin, T. W. 2019, *ApJ*, **881**, 120

Lee, E. J., & Chiang, E. 2016, *ApJ*, **817**, 90

Léger, A., Selsis, F., Sotin, C., et al. 2004, *Icar*, **169**, 499

Lopez, E. D., & Fortney, J. J. 2014, *ApJ*, **792**, 1

Madhusudhan, N., Lee, K. K. M., & Mousis, O. 2012, *ApJL*, **759**, L40

Meadows, V. S., & Barnes, R. K. 2018, in *Handbook of Exoplanets*, ed. H. J. Deeg & J. A. Belmonte (Berlin: Springer), 57

Merino, N., Aronson, H. S., Bojanova, D. P., et al. 2019, *Frontiers in Microbiology*, **10**, 780

Montet, B. T., Morton, T. D., Foreman-Mackey, D., et al. 2015, *ApJ*, **809**, 25

Morley, C. V., Fortney, J. J., Kempton, E. M. R., et al. 2013, *ApJ*, **775**, 33

Mulders, G. D., Pascucci, I., & Apai, D. 2015, *ApJ*, **814**, 130

Nettelmann, N., Fortney, J. J., Kramm, U., & Redmer, R. 2011, *ApJ*, **733**, 2

Pierrehumbert, R., & Gaidos, E. 2011, *ApJL*, **734**, L13

Pinhas, A., & Madhusudhan, N. 2017, *MNRAS*, **471**, 4355

Pinhas, A., Madhusudhan, N., Gandhi, S., & MacDonald, R. 2019, *MNRAS*, **482**, 1485

Richard, C., Gordon, I. E., Rothman, L. S., et al. 2012, *JQSRT*, **113**, 1276

Rogers, L. A., Bodenheimer, P., Lissauer, J. J., & Seager, S. 2011, *ApJ*, **738**, 59

Rogers, L. A., & Seager, S. 2010, *ApJ*, **716**, 1208

Rothman, L. S., Gordon, I. E., Barber, R. J., et al. 2010, *JQSRT*, **111**, 2139

Seager, S., Bains, W., & Hu, R. 2013, *ApJ*, **777**, 95

Seager, S., Kuchner, M., Hier-Majumder, C. A., & Militzer, B. 2007, *ApJ*, **669**, 1279

Soubiran, F., & Militzer, B. 2015, *ApJ*, **806**, 228

Southworth, J. 2011, *MNRAS*, **417**, 2166

Sugimura, E., Komabayashi, T., Hirose, K., et al. 2010, *PhRvB*, **82**, 134103

Thomas, S. W., & Madhusudhan, N. 2016, *MNRAS*, **458**, 1330

Trotta, R. 2008, *ConPh*, **49**, 71

Tsiaras, A., Waldmann, I. P., Tinetti, G., Tennyson, J., & Yurchenko, S. N. 2019, *NatAs*, **3**, 1086

Valencia, D., Guillot, T., Parmentier, V., & Freedman, R. S. 2013, *ApJ*, **775**, 10

Valencia, D., Ikoma, M., Guillot, T., & Nettelmann, N. 2010, *A&A*, **516**, A20

Wagner, W., & Pruß, A. 2002, *JPCRD*, **31**, 387

Welbanks, L., & Madhusudhan, N. 2019, *AJ*, **157**, 206

Welbanks, L., Madhusudhan, N., Allard, N. F., et al. 2019, *ApJL*, **887**, L20

Yurchenko, S. N., Barber, R. J., & Tennyson, J. 2011, *MNRAS*, **413**, 1828

Yurchenko, S. N., & Tennyson, J. 2014, *MNRAS*, **440**, 1649